

River winds and pollutant recirculation near the Manaus city in the central Amazon

Tianning Zhao¹, Jianhuai Ye^{1,9}, Igor O. Ribeiro^{2,3}, Yongjing Ma⁴, Hui-Ming Hung⁵, Carla E. Batista^{2,3}, Matthew P. Stewart¹, Patricia C. Guimarães^{2,3}, Jordi Vilà-Guerau de Arellano⁶, Rodrigo A. F. de Souza³, Alex B. Guenther⁷ & Scot T. Martin^{1,8}✉

Local atmospheric recirculation flows (i.e., river winds) induced by thermal contrast between wide Amazon rivers and adjacent forests could affect pollutant dispersion, but observational platforms for investigating this possibility have been lacking. Here we collected daytime vertical profiles of meteorological variables and chemical concentrations up to 500 m with a copter-type unmanned aerial vehicle during the 2019 dry season. Cluster analysis showed that a river-forest recirculation flow occurred for 23% (13 of 56) of the profiles. In fair weather, the thermally driven river winds fully developed for synoptic wind speeds below 4 m s^{-1} , and during these periods the vertical profiles of carbon monoxide and total oxidants (defined as ozone and nitrogen dioxide) were altered. Numerical modeling shows that the river winds can recirculate pollution back toward the riverbank. There are implications regarding air quality for the many human settlements along the rivers throughout northern Brazil.

¹School of Engineering and Applied Sciences, Harvard University, Cambridge, MA 02138, USA. ²Post-graduate Program in Climate and Environment, National Institute of Amazonian Research, Manaus, Amazonas 69060-001, Brazil. ³School of Technology, Amazonas State University, Manaus, Amazonas 69065-020, Brazil. ⁴State Key Laboratory of Atmospheric Boundary Layer Physics and Atmospheric Chemistry, Institute of Atmospheric Physics, Chinese Academy of Sciences, Beijing 100029, China. ⁵Department of Atmospheric Sciences, National Taiwan University, Taipei 10617, Taiwan. ⁶Meteorology and Air Quality Group, Wageningen University & Research, Wageningen, The Netherlands. ⁷Department of Earth System Science, University of California, Irvine, CA 92697, USA. ⁸Department of Earth and Planetary Sciences, Harvard University, Cambridge, MA 02138, USA. ⁹Present address: School of Environmental Science and Engineering, Southern University of Science and Technology, Shenzhen, Guangdong 518055, China. ✉email: scot_martin@harvard.edu

Thermal contrast in a landscape of wide rivers and adjacent forest can induce important local atmospheric circulations that manifest as river winds^{1–3}. Wide rivers throughout Amazonia typically span 5–10 km. Under sunny skies, the daytime thermal difference between warm land and cool water contributes a local tendency for air to ascend over the warm land and to descend over the cool water. The resulting horizontal pressure gradients can drive air flow at surface elevation from the river to the land. In the absence of further complicating effects of local topography and other factors, such as frequent inclement weather during the wet season and weakened thermal contrast under cloudy skies, a return wind from the land to the river can develop overhead at several hundred meters in altitude. In this way, closed recirculating sub-cells of river winds at the small mesoscale are possible. During the night, the system reverses. The land cools more rapidly than the river, and nighttime recirculation sub-cells are possible in the opposite directionality of the daytime counterparts.

In Amazonia of northern Brazil, 11 million people live in the vicinity of wide rivers (Supplementary Note 1, Fig. S1)⁴. The extent to which local winds driven by these wide rivers affect the air quality of these individuals, including the day-to-day variability of these impacts, is largely unknown, and the possible effects of these flows are not included in air quality models^{5–7}. As one example, observations aboard a boat showed that a change in surface wind direction in the late afternoon led to multifold increases in ozone (O₃) and nitrogen oxides (NO_x) concentrations⁸. Pollutant emissions from the nearby urban region of Manaus, Brazil, were advected by this river-induced atmospheric flow to the boat location^{9–11}.

River winds represent an interaction between mesoscale meteorological forcing and local landcover¹². On different days, the induced flows can vary between extremes of strong winds to entirely absent depending on the heterogeneity of the sensible heat flux and the strength and the direction of synoptic winds^{1,13–15}. Vertical profiles of meteorological variables and chemical concentrations in the lower several hundred meters of the atmosphere can in principle provide insights and understanding into the development and the effects of the altered atmospheric circulation, yet the needed data sets do not exist. Traditional measurement platforms like tethered balloons¹⁶, aircrafts^{10,17,18}, and instrumented towers^{19,20} are not suited to the collection of vertical profiles in the low atmosphere over rivers. Unmanned aerial vehicles (UAVs), in particular copter-type UAVs having take-off weights of <25 kg, represent an important capability for vertical profiles across the needed horizontal and vertical scales^{21–23}. Electrochemical sensors suitable for UAV flight can detect and quantify air pollutants at atmospherically relevant concentrations^{24,25}.

Herein, vertical profiles of meteorological and chemical data from surface elevation to 500 m were collected by a UAV during the daytime over a wide river in the central Amazon of northern Brazil in the dry season. The meteorological data were treated by a cluster analysis. The clusters were further applied to interpret the vertical profiles of air pollution, including indicators of atmospheric recirculation that effectively slowed pollutant dispersion. Implications for the air quality of nearby human populations were quantitatively examined through a pairing between the observations and an idealized, local large eddy simulation.

Results and discussion

Meteorological observations and clusters. Flights of a hovering-type hexacopter UAV were launched from a boat deck from 10:00 to 17:00 (local time; 4 h earlier than UTC) across 11 September to 9 October 2019 (Fig. 1a and b; see “Methods”). Figure 1c shows

the location of the launch site and the environs in the Rio Negro River (3.0708°S, 60.3604°W). River width varied from 3 to 13 km in this region. For the dominant wind direction, the launch site was 37.5 km downwind from Manaus, Brazil, an urban center of more than 2 million people. The launch location responded to the study requirements of capturing regional sources of pollution within the prevailing synoptic meteorology (i.e., trade winds) as well as to the practical requirements of permissions of aviation authorities for UAV flights (i.e., sufficiently far from the Manaus international airport) and the presence of police patrols against river pirates (i.e., sufficiently close to the Manaus port region). Vertical profiles of 1-m resolution were collected by the UAV once per hour from surface elevation to 500 m for 56 flights. Meteorological data of wind speed, wind direction, relative humidity, and temperature were collected. There were chemical data for 25 of the flights at 1-m resolution (Supplementary Note 2, Table S1). A zenith-pointing lidar system on the boat recorded wind speed and direction from 50 m to 2500 m at 50-m resolution.

A fuzzy c-means (FCM) clustering algorithm was applied to the vertical profiles of the radial wind components of speed and direction²⁶. The FCM algorithm identified four clusters (Supplementary Note 3, Figs. S2 and S3). This cluster count maximized the fuzzy partition coefficient and led to a meaningful interpretation of the set of clusters. The four clusters are summarized in Table 1. Complementary clustering analysis by Cartesian wind direction yielded similar results (Supplementary Note 4, Fig. S4). The degree of membership to a single cluster exceeded 0.5 for 79% (44 of 56) of the profiles (Fig. S5), and the clusters corresponded to distinct meteorological regimes²⁷. The cluster centroids of wind direction and wind speed are plotted in Fig. 2a and b, respectively. Cluster centroids of relative humidity and temperature are plotted in Figure S6. The data sets of the lidar on the boat further supported the four cluster assignments (Supplementary Note 5, Figs. S7 and S8).

Cluster 1, prevalent for fair-weather cumulus clouds over the land, had the distinguishing feature of a complete reversal of wind direction at mid-height. The centroid for this cluster had westerlies below 100 m that transitioned into easterlies above 300 m (Fig. 2a and b). Correspondingly, there was a local minimum in the wind speed at 200 m. Trade winds (i.e., easterlies) dominated the wind field above 300 m, and the local circulatory flow of the river-forest landscape affected the wind field at lower altitudes. These observations represent a canonical example of strong local circulatory flows of a closed sub-cell^{2,12,15}. The raw meteorological data for flights in cluster 1 are plotted in Fig. S9. During periods of cluster 1, satellite images show that there were typically no clouds over the river (Fig. 2c). The air rising over the land desiccated, and it subsequently descended without cloud formation over the rivers²⁸.

Interestingly, the sub-cell of the river winds for cluster 1 ran as easterlies and westerlies. The expectation given the river orientation and the positioning of the boat could be for northerlies and southerlies, at least for the ideal situation of a river breeze (Fig. 1c). An ideal situation corresponds to no regional winds, uniform heating at both riverbanks, and consistent east-west river orientation. However, in the real case, the physics were more mixed, including additional simultaneous forcing by both synoptic and river-forest factors. Easterly trade winds were present, the southern bank of the river was usually warmer than the northern bank, and the river orientation around flowed in the direction of northwest to southeast, instead of west to east, on a slightly larger spatial scale (Fig. 1c). These several factors contributed to the difference between the expectations for ideal river breezes and the observations of real river winds produced by the physics of simultaneous mixed forcing.

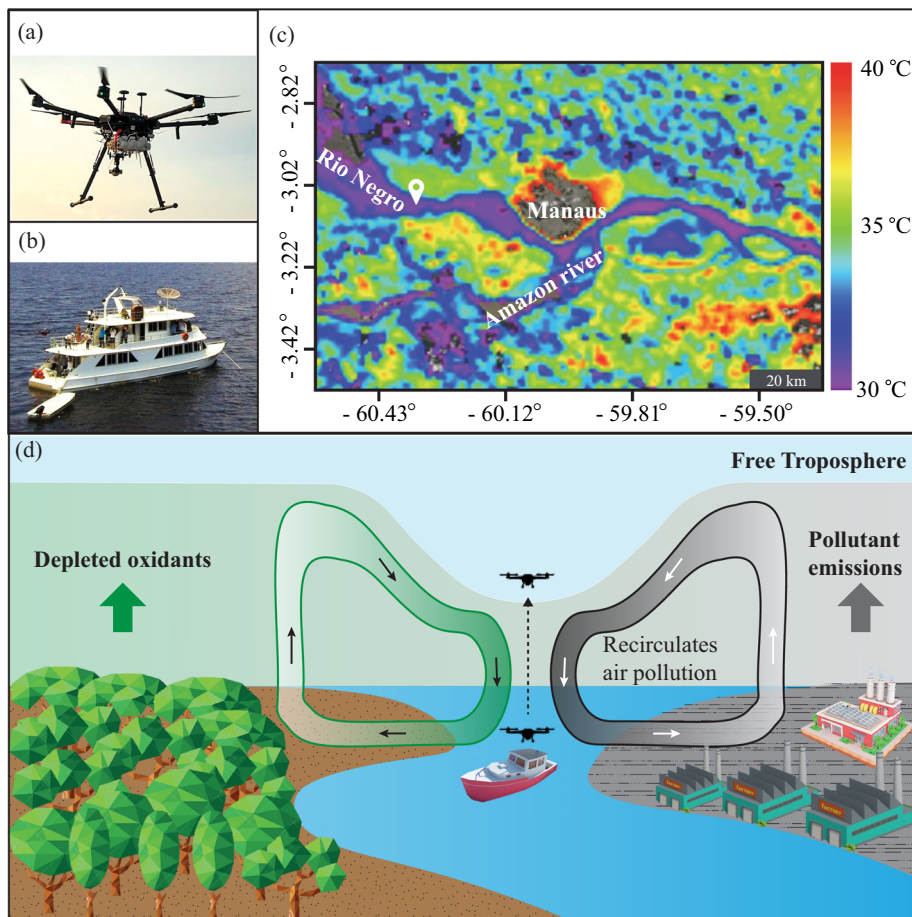


Fig. 1 Conceptual overview of river winds and details of field campaign. **a** Photograph of the UAV. The sensor package was mounted to the UAV underside. **b** Photograph of the boat platform from which the UAV was launched and retrieved during the campaign. The boat was positioned at the white marker (3.0708° S, 60.3604° W) of panel (c). **c** Surface temperatures on a fair weather day⁴³. The data for the false-color image were taken by the *Aqua* satellite at 13:30 (LT) over Manaus, Brazil, in the central Amazon on 26 September 2019. Satellite image credit: NASA’s Earth Observatory. **d** Representation of thermally driven recirculatory flow of river winds and reduced rates of pollutant dispersion in a river-forest landscape.

Table 1 Clustering analysis of the vertical profiles of meteorological data.

Cluster	Occurrence	Synoptic wind speeds (m s ⁻¹)	Other characteristics
1, Strong local circulatory flows of river winds.	23% (13)	2.5	Fair weather
2, No apparent circulatory flow. Flow over river appears same as over forest.	21% (12)	>4	Fair weather
3, Weak to perturbed local circulatory flows of river winds.	25% (14)	<4	Cirrus and high-altitude stratus clouds
4, Other types of flows.	31% (17)	2.5	Incliment weather and other factors

The parenthesized numbers indicate how many profiles out of 56 occurred in each cluster.

The wind roses of other research sites away from the rivers show that westerlies are rare in the central Amazon because of the prevailing equatorial trade winds (Fig. S10). The observation of westerly surface winds for cluster 1 is thus a direct consequence of the induced flows that manifested as river winds.

Cluster 2, which like cluster 1 also occurred at times of fair-weather cumulus clouds, was characterized by fast (>4 m s⁻¹) and uniform easterlies of the trade winds from the surface elevation up to 500 m throughout the day (Fig. 2a and b). The characteristic signs of strong local circulatory flows of river winds that were apparent in the meteorology of cluster 1 were absent for cluster 2. Instead, the vertical profiles were as they occur over forested regions under the influence of the trade winds. Although the

satellite observations of fair-weather cumulus clouds might suggest favorable weather for thermally induced circulation over the river (cluster 2, Fig. 2d), the pressure gradient at the synoptic scale was large enough, as reflected in the fast winds, that the air flow was dominated by this synoptic forcing²⁹. The physics of local circulation were overwhelmed.

The characteristics of cluster 3 were similar to those of cluster 2 in terms of easterlies and the absence of signs of strong local circulatory flows. The wind speeds (<4 m s⁻¹), however, were less than those of cluster 2, and the associated satellite images also differed between the two clusters. For cluster 3, cirrus clouds were typically present (Fig. 2e). They reduced surface insolation, resulting in a smaller temperature difference between the land

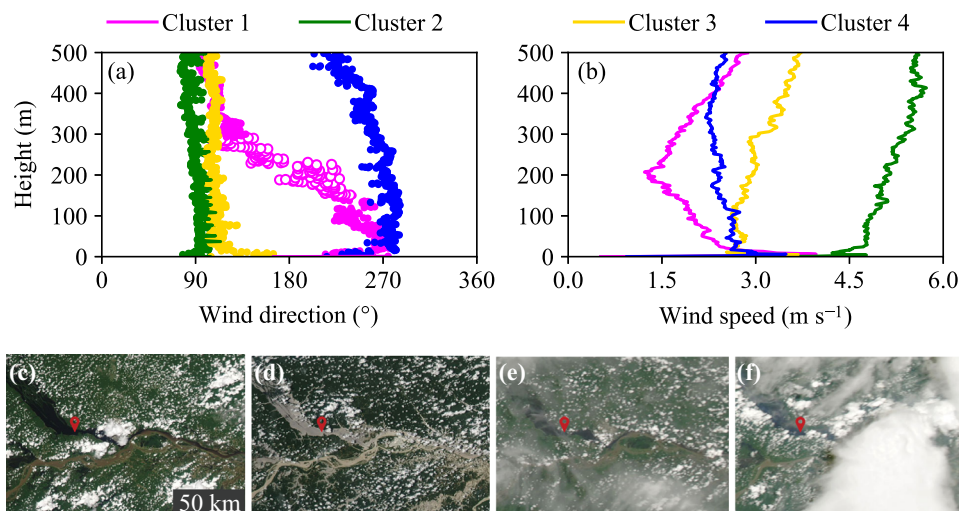


Fig. 2 Four meteorological clusters identified by analysis of 56 vertical profiles of data. **a, b** Cluster centroids of wind direction (degrees) and wind speed (m s^{-1}) from surface elevation to 500 m. Open circles indicate wind speeds slower than 2 m s^{-1} , for which the wind direction was less certain.⁴³ **c–f** Satellite images of cloud coverage that were typical of clusters 1, 2, 3, and 4, respectively⁴³. Images were taken by the *Aqua* satellite at 13:30 (LT) on 26 September 2019, 30 September 2019, 1 October 2019, and 8 October 2019. The imaged rivers correspond to those apparent in Fig. 1c. The boat was positioned at the red marker. Satellite image credit: NASA’s Earth Observatory.

and the river³⁰. The development of the thermally induced local flows of river winds has two requirements¹: (1) the temperature difference between the land and the river and hence the buoyancy of the air over them must induce a sufficiently large horizontal pressure gradient for horizontal air movement and (2) the pressure gradient from the synoptic winds must be sufficiently small that the local pressure gradient is retained. For cluster 3, both requirements were met but only weakly. Forcings from the synoptic winds and the thermal effects from the river-forest landscape simultaneously affected the atmospheric flow, and they did so with high variability. As a result, although there were similar centroids of wind direction between clusters 2 and 3 (Fig. 2a), there was a signature difference between them of low variability around the centroid of wind direction for cluster 2 compared to a high variability for cluster 3 (Fig. S11).

Cluster 4 had weak westerlies in the surface region. Above 300 m, there was a drift southerly to the point of maximum UAV altitude (i.e., 500 m). The wind speed of the centroid was 2.5 m s^{-1} from the surface elevation to 500 m. There were two main features that distinguished cluster 4 from cluster 1: (1) the drift of wind direction was above 300 m and (2) the wind speed did not have a minimum at mid-height. These characteristics of cluster 4 might be related to several different possibilities, including various types of strong convection. For instance, 47% (8 of 17) of the profiles in cluster 4 occurred proximate to the arrival or departure of inclement weather, as reflected by the presence of large convective clouds in the satellite images (Fig. 2f).

The remainder of the analysis herein focuses on cluster 1, which was observed in 23% of the flights, to explore links between river winds and recirculation of local pollution.

Vertical profiles of pollutant concentrations. The coupling represented by cluster 1 between pollution and local recirculation is depicted conceptually in Fig. 1d. Among 25 chemical profiles, three of them fell within cluster 1. Vertical profiles of pollutant concentrations are plotted in Fig. 3 for a representative flight of cluster 1. Changes in wind direction at mid-altitude accompanied increases in the concentrations of carbon monoxide (CO) and total oxidants (O_x , defined as O_3 and NO_2). Normalized gradients in species concentration from the surface elevation to 500 m for

each flight were used in the analysis (see “Methods”). Scatter in wind direction from 100 to 200 m arose from the low wind speeds that accompanied the reversal in wind direction across this altitude range (gray region, Fig. 3). Arrows in Fig. 3 demarcate inflection points in the pollutant concentrations at 180 m. The altitude of the increased concentrations aligned with the height at which the wind direction changed in the circulation cell.

The UAV measurements of the wind speed and the wind direction were confirmed by the lidar observations aboard the boat. The red points in Fig. 3 show the lidar observations, which had a vertical resolution of 50 m. The 1-m UAV data were smoothed to 50 m to allow for the comparison (blue line, Fig. 3). Typical daytime boundary layer heights approach 1500 m during dry season in the central Amazon³¹. Figure S12 further shows the lidar data from surface elevation to 1500 m during the flight of Fig. 3. At altitudes far above the river winds, wind direction was unchanged, and wind speed continuously increased, as expected.

The vertical profiles of pollutant concentrations in Fig. 3 can be explained by strong local circulatory flows of a closed sub-cell over a river-forest landscape when there were nearby pollutant emissions. As depicted in Fig. 1d, polluted air from the land source was transported from the surface to above 300 m in the branch of upward convection in the circulation cell, and this pollution then descended over the river to below 300 m in the downward branch of the cell. Back-trajectories indicate that the air originated to the southeast where there were many wood-burning brick kilns that had high CO emissions nearby the river (Fig. S13)³². One group of brick kilns was within 10 km of the UAV launch location. There were also biomass burning hotspots on these days further along the back-trajectories from 80 to 120 km, representing 4–6 h of transport time, and biomass burning was also a strong source of CO emissions³³.

For all clusters, the CO concentration decreased with height. Vertical profiles are plotted in Fig. S14 for flights representative of each cluster (i.e., based on the degree of membership). The complete set of individual profiles is plotted in Figure S15. A decrease in CO concentration with altitude for all clusters is consistent with other Amazon observations of CO concentrations across a larger altitude range from 500 m to 3000 m^{17,34}. In the case of cluster 1, there was an inflection point of CO concentration at mid-height. Figure 3 shows that the

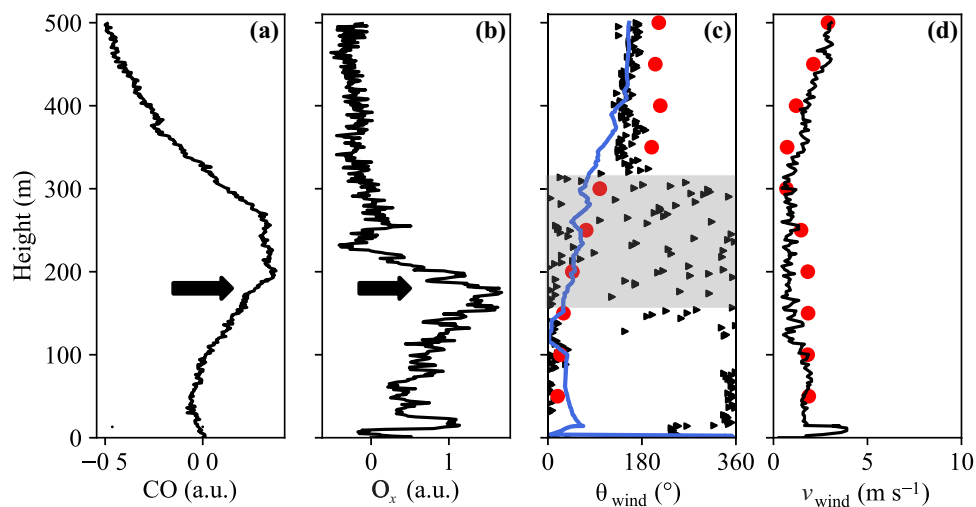


Fig. 3 Vertical profiles of normalized CO and O_x concentrations, along with meteorological parameters, from surface elevation to 500 m for an individual UAV flight at 13:53 (LT) on 7 October 2019 (flight 47, representative flight of cluster 1). **a** Normalized CO concentration (CO, a.u.). **b** Normalized O_x concentration (O_x , a.u.). **c** Wind direction (θ_{wind} , degrees). **d** Wind speed (v_{wind} , $m\ s^{-1}$). Horizontal arrows show inflection points in the vertical profiles. Lidar observations from the boat are in overlay as red points. The gray region highlights the altitude band across which low wind speeds occurred, and wind direction was less certain (cf. Fig. 2). For comparison, the blue line is a 50-m moving average of the UAV data.

O_x concentrations likewise decreased and then increased across 100 m to 250 m for cluster 1. Wind speed and wind direction changed across the same altitude range (Fig. 2). Although O_x was lost by dry deposition to both the forest canopy and the river surface, the rate of dry deposition to the water surface was lower³⁵. The local circulation uplifted O_x -depleted air from the nearby land surface, leading to reduced O_x concentrations for the altitude at which the sub-cell descended over the river (Fig. 1d). Supplementary Note 6 discusses that a possible alternative explanation of differences in dilution or mixing of buoyant airmasses was not supported by the lidar data (Fig. S16). The O_x concentration also did not change with altitude for clusters 2, 3, and 4.

The qualitative features of Fig. 1d for atmospheric recirculation of local emissions that effectively slows pollutant dispersion were explored quantitatively within a large eddy simulation (LES). The setup and parameters were constructed as an idealized counterpart to the actual conditions of cluster 1 in the absence of synoptic winds (see “Methods”)^{36,37}. In the idealized simulation, CO was continuously emitted from a nearby point source on land. The results also hold for tracers other than CO provided that they have an atmospheric lifetime that also exceeds the transport time through the circulation cell. The simulation represented an idealized treatment of many local factors as a strategy for gaining insight into the governing processes and the quantitative extent of slowed pollutant dispersion for nearby human populations.

A baseline LES was run for a homogeneous landscape of a forest in the absence of a river (Fig. 4a). For this reference simulation, the pollution from the point source was transported upward, there was no recirculation back to the surface, and the pollution was dispersed by dilution and entrainment away from the riparian zone of human settlement. An experiment LES was conducted by altering the landscape to include a river (Fig. 4b). For this simulation, a thermally driven closed sub-cell of strong local circulatory flows formed over the river-forest landscape. The pollution was carried upward in this sub-cell over the land, mixed toward the middle of the river, and recirculated back to the nearby surface (Fig. 4b). Figure 1a graphically represents this type of sub-cell transport.

Vertical profiles at 25% and 50% along the horizontal transect of the river were used to simulate UAV sampling³⁸. The pollution concentration reached a maximum value at mid-height (Fig. 4c, solid lines). This simulated behavior is consistent with the observations plotted in Fig. 3. Vertical profiles of the horizontal speeds of the simulated river winds are plotted in Fig. 4d. The maximum of the simulated speed was $2\ m\ s^{-1}$, and its direction flipped at $\sim 250\ m$. Both of these simulation results are in good agreement with the observations for cluster 1 (Fig. 2a, b). The LES-simulated maximum height of the sub-cell of the river winds also agreed with an earlier parameterized treatment within a Eulerian chemical transport model³⁹.

Recirculation to the surface riparian zone rather than transport away from it implies greater air pollution in the zone of human settlement. The extent of increased air pollution because of reduced pollutant dispersion was assessed in the simulation by taking a vertical profile at the riverbank. In the simulation, the pollution concentration at the riverbank approximately doubled in the presence compared to in the absence of the LES-simulated recirculation (Fig. 4c, blue lines).

Conclusions. The vertical profiles of meteorological variables sampled by UAV flights over a wide river in the central Amazon corresponded to a thermally driven closed sub-cell of strong local circulatory flows, constituting river winds, over the river-forest landscape for 23% (13 of 56) of the flights during the daytime of the dry season. The height of the transition layer for river winds varied from 150 to 300 m over the surface elevation among different days compared to 1000 to 1500 m for the boundary layer height. Synoptic winds slower than $4\ m\ s^{-1}$ and an absence of high-altitude clouds favored the development of the sub-cell of river winds. By comparison, for 21% of the flights river winds were not observed, and during these times strong synoptic trade winds prevailed. More complex behavior than these two limiting extremes was observed during the other flights (56%), in part because of complex mesoscale meteorology such as inclement weather and in part because of mixed physics at times of simultaneous forcing by both synoptic and river-forest factors.

This study provides the first in-situ vertical profile measurements of river winds in central Amazonia. Prior work on this

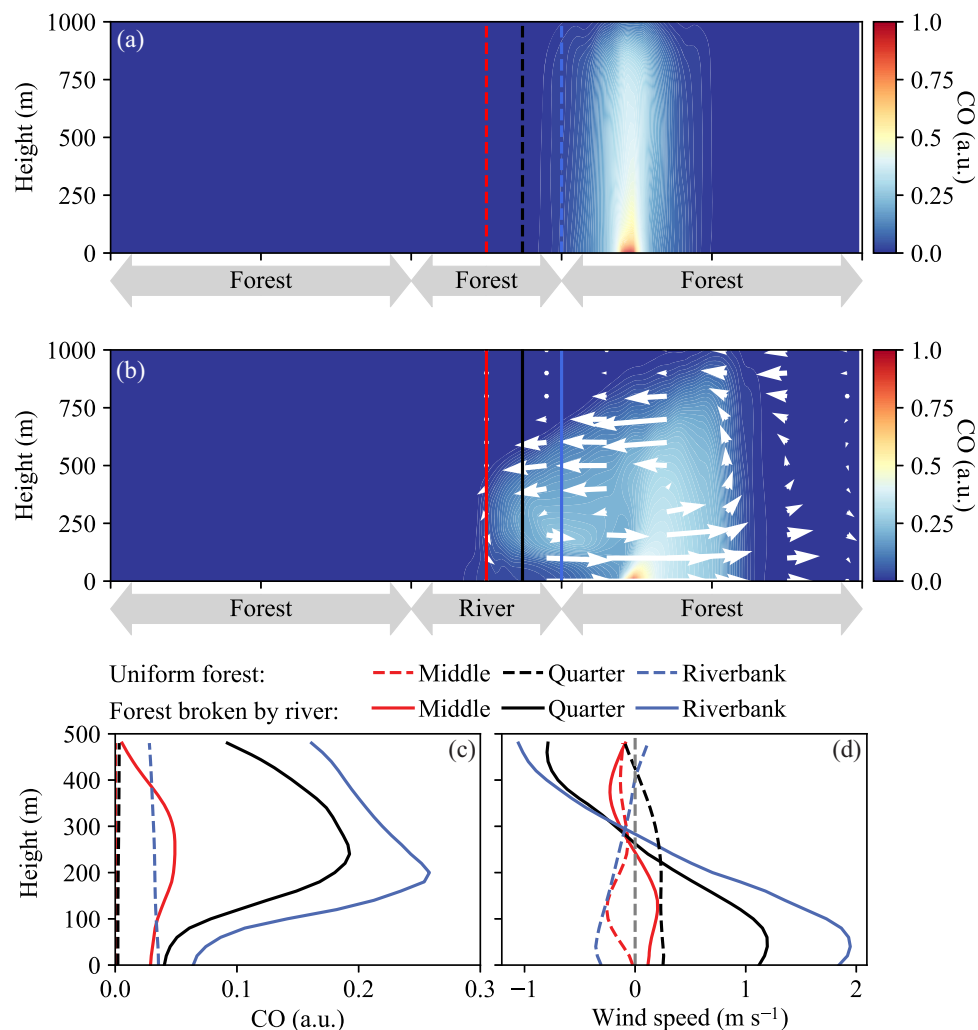


Fig. 4 Large eddy simulation (LES) representative of cluster 1. The simulation ran for 3 h, and the results were averaged over the last hour. **a** Forested landscape. **b** Forested landscape broken by a river of 5-km width. White arrows depict the simulated wind field. **c** Vertical profiles of normalized CO concentration (CO, a.u.). Profiles over the riverbank, 25% across the river, and 50% across the river are represented by blue, black, and red lines, respectively. Dashed and solid lines represent the results for the landscapes of panels **a** and **b**, respectively. **d** Vertical profiles of wind speed (m s⁻¹). Positive values of wind speed represent a wind direction from the middle of the river toward the forest.

topic was limited to simulation results constrained by on-shore data. The dataset collected with sensors onboard unmanned aerial vehicles as well as wind lidar fills the gap between theoretical results and extrapolation from surface measurements. The coupling of river winds to the distribution of atmospheric pollutants was examined, both in the data sets and in complementary large-eddy simulations. Air quality models can be improved by quantitatively accounting for river winds (at present they do not), and the models can be tested against the data constraints of this study for the role of river winds in the distribution of atmospheric pollutants.

The impacts of local recirculation can be considerable in certain regions. Human settlement throughout northern Brazil is strongly favored along rivers, so the effects of the coupling between pollution dispersion and river winds on local air quality and human health can be important when certain small mesoscale regimes prevail on some days. Regional numerical air quality models today do not incorporate these river-derived processes. Moreover, on days that river winds prevail, the extrapolation of any measurements of chemical concentrations over the river surface or land nearby its banks to a larger regional scale should be considered cautiously. The local circulations can

change the spatial pattern and residence time of locally emitted pollution. Linked epidemiological studies that integrate the role of river recirculation in explaining the spatial micro-heterogeneity of human health outcomes, including environmental equity, should be considered in the future.

The ongoing migration of biomass burning deeper into Amazonia where rivers are abundant and human population along the rivers is prevalent adds urgency to efforts to understand the impact of river winds on air pollution⁴⁰. There has been a large and sustained uptick in agricultural and deforestation fires as additional pollution sources in the interior of the Amazon region over the past decade^{41,42}. This phenomenon has unknown health consequences and tie-ins to local meteorology, including river winds. This pattern of biomass burning differs from earlier decades of historical deforestation that was largely restricted along the southern and eastern borders of the Amazon region rather than also in its interior where the population is distributed primarily along rivers. There is a distinct possibility that the coupling between polluted river winds and air quality is degrading public health of the vulnerable populations of northern Brazil. Air pollution management strategies, including air pollution monitoring locations and air quality modeling, should

incorporate the effects of river winds into pollution mitigation strategies and policies.

Methods

UAV flights. A hexacopter UAV (Matrice 600, DJI) was used in this study (Fig. 1c)²². Telemetry of latitude, longitude, and altitude was based on the Global Positioning System (GPS). The operational capability of the UAV limited the flight time to <30 min. The maximum ascending and descending speeds of the UAV were 5 m s⁻¹ and 3 m s⁻¹, respectively. The maximum altitude was 500 m above local ground, as restricted by manufacturer geofencing. During the measurement, the UAV ascended at a speed of 1 m s⁻¹ from the surface to 500 m. This ascending speed was selected to minimize the impacts of UAV-induced turbulence on sensor measurements^{22,44}. The hourly UAV flight routine at the measurement location was interrupted on some days because of weather or other unexpected technical issues.

Meteorological measurements. Wind measurements, including vertical profiles of wind direction and wind speed, were performed by a UAV-wind sensor system (Model UAV6000, ZOGLAB Microsystem Co.). The accuracy of wind speed was 0.5 m s⁻¹. The accuracy of wind direction was 3° for wind speeds faster than 2 m s⁻¹ (Supplementary Note 7). Temperature (±0.2 °C) and relative humidity (±2.5% RH) were also measured.

A lidar (Model LWR2500, ZOGLAB Microsystem Co.) on the boat recorded altitude-resolved horizontal wind speed and direction from 50 m to 2500 m. The vertical resolution was 50 m. The accuracy for the wind speed was 0.5 m s⁻¹. The accuracy for the wind direction was 3°. Data were averaged for one minute. Relative wind direction changes compared to the measurement at the lowest altitude (50 m) were used in the analysis to compensate for boat rotation.

Chemical sensing. The chemical sensor package was affixed to the underside of the UAV. This position protected it from overheating under solar illumination. The sensor package was housed in a weather-proof plastic enclosure (20.1 cm × 15.5 cm × 7.9 cm). Electrochemical sensors measured CO and O_x (Table S2). Data were recorded every 1 s. Calibration for temperature compensated for the temperature gradient with altitude during flight (Supplementary Note 8, Fig. S17, Table S3).

The calibration of the electrochemical sensors was difficult under the tropical field conditions when operated from the boat, and drift in sensor response was observed across several days. Drift is well documented for electrochemical sensors^{24,25,38}. The drift, however, was sufficiently small that precision was maintained across the measurements for the flights of a single day. In this case, normalized data from 0 to 1 based on the gradient for each day allowed qualitative patterns to be compared across days, as follows: $\delta_z = (C_z - C_0)/C_0$ where δ_z is a normalized datum at altitude z , C_z is the apparent concentration measured at altitude z , and C_0 is the apparent surface concentration.

Across the campaign, the average surface concentrations for CO and O_x were 223 ppb and 18 ppb, respectively. The O_x concentration was an upper limit of the O₃ concentration. These CO and O_x concentrations were in the same range as those of aircraft measurements at 500 m that were carried out in the GoAmazon2014/5 campaign in the same geographical region (Table S4). In that study, mid-day values of ozone ranged from 20 to 60 ppb in the dry season.

Other data sets. Daily satellite images of cloud coverage were acquired from the Terra (overflight time of 10:30, LT), Suomi (13:30, LT), and Aqua (13:30, LT)⁴³. Daily maps of regional biomass burning were obtained from the Brazilian National Institute for Space Research²⁴. Back trajectories of air parcels to the sampling location at 100, 300, and 500 m were calculated using the Real-time Environmental Applications and Display sYstem (READY) of the Hybrid Single-Particle Lagrangian Integrated Trajectory (HYSPLIT) model^{25,45} (Table S5).

Large eddy simulations. Transport was simulated using the Dutch Atmospheric Large Eddy Simulation (DALES) (Version 4.1)³⁶. DALES has been validated in the Amazon region³⁷. The domain setup is depicted in Fig. S18. The river width was 5 km in a domain width of 25 km. There was a periodic lateral boundary condition. The forest size in the periodic domain was sufficiently wide to isolate the river in each cell. There was a point source of CO emissions (0.13 mg m⁻² s⁻¹ or 100 ppb m s⁻¹) that was 2.5 km inland (Fig. S18). The parameters were optimized to reproduce the meteorological observations of the campaign^{37,44} (Table S6). Wind speeds driven by a thermal contrast of 2 °C in the river-forest landscape should range from 1.5 to 3 m s⁻¹^{36,37,46–50}. For comparison, a satellite image shows a river-land temperature difference of 4 °C during the period of measurements (Fig. 1a). The simulation initiated at 12:00 (LT) and ran for 3 h. For further analysis, the results averaged over the last hour were used. The simulated concentrations were normalized from 0 to 1 across the minimum and maximum values.

Data availability

The data of the vertical profiles from UAV and lidar measurements are available at <https://doi.org/10.7910/DVN/VSYM5>.

Code availability

The source code used for Large Eddy Simulation is available at: <https://github.com/dalessteam/dales>

Received: 26 April 2021; Accepted: 9 September 2021;

Published online: 01 October 2021

References

- Crosman, E. T. & Horel, J. D. Sea and lake breezes: a review of numerical studies. *Boundary-Layer Meteorol.* **137**, 1–29 (2010).
- Miller, S. T. K., Keim, B. D., Talbot, R. W. & Mao, H. Sea breeze: STRUCTURE, Forecasting, and impacts. *Rev. Geophys.* **41**, 1011 (2003).
- Simpson, J. E. *Sea Breeze and Local Winds* (Cambridge University Press, 1994).
- IBGE. *Brazilian Institute of Geography and Statistics*, <https://www.ibge.gov.br> (2021).
- David, L. M. & Nair, P. R. Diurnal and seasonal variability of surface ozone and NO_x at a tropical coastal site: Association with mesoscale and synoptic meteorological conditions. *J. Geophys. Res.* **116**, D10303 (2011).
- Li, W., Wang, Y. X., Bernier, C. & Estes, M. Identification of sea breeze recirculation and its effects on ozone in Houston, TX, during DISCOVER-AQ 2013. *J. Geophys. Res.* **125**, e2020JD033165 (2020).
- Ma, Y. M. & Lyons, T. J. Recirculation of coastal urban air pollution under a synoptic scale thermal trough in Perth, Western Australia. *Atmos. Environ.* **37**, 443–454 (2003).
- Trebs, I. et al. Impact of the Manaus urban plume on trace gas mixing ratios near the surface in the Amazon Basin: Implications for the NO-NO₂-O₃ photostationary state and peroxy radical levels. *J. Geophys. Res.* **117**, D05307 (2012).
- Kuhn, U. et al. Impact of Manaus city on the Amazon green ocean atmosphere: ozone production, precursor sensitivity and aerosol load. *Atmos. Chem. Phys.* **10**, 9251–9282 (2010).
- Martin, S. T. et al. The Green Ocean Amazon experiment (GoAmazon2014/5) observes pollution affecting gases, aerosols, clouds, and rainfall over the rain forest. *Bull. Amer. Meteorol. Soc.* **98**, 981–997 (2017).
- Shrivastava, M. et al. Urban pollution greatly enhances formation of natural aerosols over the Amazon rainforest. *Nature Communications* **10**, 1046 (2019).
- Betts, A. et al. The Amazonian boundary layer and mesoscale circulations. *Amazonia and Global Change. Geophysical Monograph* <https://doi.org/10.1029/2008GM000720> (2009).
- Fitzjarrald, D. R. et al. Spatial and temporal rainfall variability near the Amazon-Tapajós confluence. *J. Geophys. Res.* **113**, G00B11 (2008).
- Germano, M. F. & Oyama, M. D. Local circulation features in the eastern Amazon: high-resolution simulation. *J. Aerosp. Technol.* **12**, e0820 (2020).
- Silva Dias, M. A. F., Silva Dias, P. L., Longo, M., Fitzjarrald, D. R. & Denning, A. S. River breeze circulation in eastern Amazonia: observations and modelling results. *Theor. Appl. Climatol.* **78**, 111–121 (2004).
- Greco, S., Ulancki, S., Garstang, M. & Houston, S. Low-level nocturnal wind maximum over the central Amazon basin. *Bound-Lay. Meteorol.* **58**, 91–115 (1992).
- Andreae, M. O. et al. Carbon monoxide and related trace gases and aerosols over the Amazon Basin during the wet and dry seasons. *Atmos. Chem. Phys.* **12**, 6041–6065 (2012).
- Fan, M. et al. Comparison of aircraft measurements during GoAmazon2014/5 and ACRIDICON-CHUVA. *Atmos. Meas. Tech.* **13**, 661–684 (2020).
- Andreae, M. O. et al. The Amazon tall tower observatory (ATTO): overview of pilot measurements on ecosystem ecology, meteorology, trace gases, and aerosols. *Atmos. Chem. Phys.* **15**, 10723–10776 (2015).
- Martin, S. T. et al. An overview of the Amazonian aerosol characterization experiment 2008 (AMAZE-08). *Atmos. Chem. Phys.* **10**, 11415–11438 (2010).
- Stewart, M. P. & Martin, S. T. *Unmanned Aerial Vehicles*, Ch. 2 (Nova Science Publishers, Hauppauge, New York, 2020).
- Guimarães, P. et al. Vertical profiles of ozone concentration collected by an unmanned aerial vehicle and the mixing of the nighttime boundary layer over an Amazonian urban area. *Atmosphere* **10**, 599 (2019).
- Liu, B. et al. Vertical profiling of fine particulate matter and black carbon by using unmanned aerial vehicle in Macau, China. *Sci. Total Environ.* **709**, 136109 (2020).
- Cross, E. S. et al. Use of electrochemical sensors for measurement of air pollution: correcting interference response and validating measurements. *Atmos. Meas. Tech.* **10**, 3575 (2017).

25. Spinelle, L., Gerboles, M., Villani, M. G., Alexandre, M. & Bonavitaola, F. Field calibration of a cluster of low-cost available sensors for air quality monitoring. Part A: Ozone and nitrogen dioxide. *Sensor. Actuat. B-Chem.* **215**, 249–257 (2015).
26. Bezdek, J. C., Ehrlich, R. & Full, W. FCM: The fuzzy c-means clustering algorithm. *Comput. Geosci.* **10**, 191–203 (1984).
27. Darby, L. S. Cluster analysis of surface winds in Houston, Texas, and the impact of wind patterns on ozone. *J. App. Meteorol.* **44**, 1788–1806 (2005).
28. Ramos da Silva, R., Gandu, A. W., Sá, L. D. A. & Silva Dias, M. A. F. Cloud streets and land–water interactions in the Amazon. *Biogeochemistry* **105**, 201–211 (2011).
29. Sozzi, R., Favaron, M. & Georgiadis, T. Method for estimation of surface roughness and similarity function of wind speed vertical profile. *J. Appl. Meteorol.* **37**, 461–469 (1998).
30. Lee, J., Yang, P., Dessler, A. E., Gao, B.-C. & Platnick, S. Distribution and radiative forcing of tropical thin cirrus clouds. *J. Atmos. Sci.* **66**, 3721–3731 (2009).
31. Carneiro, R. G. & Fisch, G. Observational analysis of the daily cycle of the planetary boundary layer in the central Amazon during a non-El Niño year and El Niño year (GoAmazon project 2014/5). *Atmos. Chem. Phys.* **20**, 5547–5558 (2020).
32. de Sa, S. S. et al. Contributions of biomass-burning, urban, and biogenic emissions to the concentrations and light-absorbing properties of particulate matter in central Amazonia during the dry season. *Atmos. Chem. Phys.* **19**, 7973–8001 (2019).
33. Ribeiro, I. O. et al. Biomass burning and carbon monoxide patterns in Brazil during the extreme drought years of 2005, 2010, and 2015. *Environ. Poll.* **243**, 1008–1014 (2018).
34. Sachse, G. W., Harriss, R. C., Fishman, J., Hill, G. F. & Cahoon, D. R. Carbon monoxide over the Amazon Basin during the 1985 dry season. *J. Geophys. Res.* **93**, 1422 (1988).
35. Wesely, M. L. Parameterization of surface resistances to gaseous dry deposition in regional-scale numerical models. *Atmos. Environ.* **23**, 1293–1304 (1989).
36. Heus, T. et al. Formulation of the dutch atmospheric large-eddy simulation (DALES) and overview of its applications. *Geosci. Model. Dev.* **3**, 415–444 (2010).
37. Ouwersloot, H. G. et al. On the segregation of chemical species in a clear boundary layer over heterogeneous land surfaces. *Atmos. Chem. Phys.* **11**, 10681–10704 (2011).
38. Ma, Y. et al. Optimization and representativeness of atmospheric chemical sampling by hovering unmanned aerial vehicles over tropical forests. *Earth Space Sci.* <https://doi.org/10.1029/2020EA001335> (2021).
39. Medeiros, A. S. S. et al. River breezes for pollutant dispersion in GoAmazon2014/5. *Atmos. Chem. Phys. Discuss.* **2018**, 1–28 (2018).
40. Davidson, E. A. et al. The Amazon basin in transition. *Nature* **481**, 321–328 (2012).
41. Amigo, I. The Amazon's fragile future. *Nature* **578**, 505–507 (2020).
42. Farias, E. *Amazônia em Chamas 20: Fumaça das queimadas encobre Manaus*, <https://amazoniareal.com.br/amazonia-em-chamas-20-fumaca-das-queimadas-encobre-manaus-09-09-2020/> (2020).
43. Worldview. *Worldview*, <https://worldview.earthdata.nasa.gov> (2020).
44. Guimarães, P. et al. Vertical profiles of atmospheric species concentrations and nighttime boundary layer structure in the dry season over an urban environment in central Amazon collected by an unmanned aerial vehicle. *Atmosphere* **11**, 1371 (2020).
45. Wei, P. et al. Impact analysis of temperature and humidity conditions on electrochemical sensor response in ambient air quality monitoring. *Sensors* **18**, 59 (2018).
46. Worldview. *Worldview*, <https://worldview.earthdata.nasa.gov> (2020).
47. INPE. *Instituto Nacional de Pesquisas Espaciais (INPE)*, <http://www.inpe.br/queimadas/bdqueimadas/> (2020).
48. Rolph, G., Stein, A. & Stunder, B. Real-time environmental applications and display system: READY. *Env. Model. Softw.* **95**, 210–228 (2017).
49. Stein, A. et al. NOAA's HYSPLIT atmospheric transport and dispersion modeling system. *Bull. Amer. Meteorol. Soc.* **96**, 2059–2077 (2015).
50. van Heerwaarden, C. C. & Vila-Guerau de Arellano, J. V. Relative humidity as an indicator for cloud formation over heterogeneous land surfaces. *J. Atmos. Sci.* **65**, 3263–3277 (2008).

Acknowledgements

This work was funded by the Division of Atmospheric and Geospace Sciences (AGS) of the USA National Science Foundation (AGS-1829025 and AGS-1829074). The Brazilian Federal Agency for Support and Evaluation of Graduate Education (CAPES), the Brazilian National Council for Scientific and Technological Development (CNPq), and the Harvard Climate Change Solutions Fund are acknowledged. Jianhui Ye acknowledges support from a postdoctoral fellowship from the Natural Sciences and Engineering Research Council of Canada and a fellowship in Environmental Chemistry from the Dreyfus Foundation. ZOGLAB Microsystem Co. (Hangzhou, China) loaned the UAV6000 and the LWR2500 for the period of measurements. Technical support of the wind measurements during the campaign by Mr. Jian Wang and Mr. James Sun from ZOGLAB Microsystem Co. is acknowledged. The Brazilian Air Force through the Department of Airspace Control (DECEA) and the National Civil Aviation Agency (ANAC) is acknowledged for the flight authorizations and support during the scientific experiment.

Author contributions

A.G., R.S., and S.M. designed the field program; T.Z., J.Y., C.B., I.R., P.G., and M.S. conducted the field measurements; T.Z. analyzed the measurement data; H.M. mentored the chemical sensor package; T.Z., J.Y., Y.M., J.V., and S.M. designed, conducted, and interpreted the large eddy simulations; and T.Z. and S.T.M. wrote the manuscript in collaboration with all co-authors.

Competing interests

The authors declare no competing interests.

Additional information

Supplementary information The online version contains supplementary material available at <https://doi.org/10.1038/s43247-021-00277-6>.

Correspondence and requests for materials should be addressed to Scot T. Martin.

Peer review information *Communications Earth & Environment* thanks Patricia Cleary, Fredrik Jansson and the other, anonymous, reviewer(s) for their contribution to the peer review of this work. Primary Handling Editors: Emma Liu, Clare Davis.

Reprints and permission information is available at <http://www.nature.com/reprints>

Publisher's note Springer Nature remains neutral with regard to jurisdictional claims in published maps and institutional affiliations.



Open Access This article is licensed under a Creative Commons Attribution 4.0 International License, which permits use, sharing, adaptation, distribution and reproduction in any medium or format, as long as you give appropriate credit to the original author(s) and the source, provide a link to the Creative Commons license, and indicate if changes were made. The images or other third party material in this article are included in the article's Creative Commons license, unless indicated otherwise in a credit line to the material. If material is not included in the article's Creative Commons license and your intended use is not permitted by statutory regulation or exceeds the permitted use, you will need to obtain permission directly from the copyright holder. To view a copy of this license, visit <http://creativecommons.org/licenses/by/4.0/>.

© The Author(s) 2021